

# Towards Exascale for Wind Energy Simulations

Misun Min<sup>1</sup>, Michael Brazell<sup>2</sup>, Ananias Tomboulides<sup>3</sup>, Matthew Churchfield<sup>4</sup>, Paul Fischer<sup>1,5,6</sup> and Michael Sprague<sup>4</sup>

## Abstract

We examine large-eddy-simulation modeling approaches and computational performance of two open-source computational fluid dynamics codes for the simulation of atmospheric boundary layer (ABL) flows that are of direct relevance to wind energy production. The first is NekRS, a high-order, unstructured-grid, spectral element code. The second, AMR-Wind, is a block-structured, second-order finite-volume code with adaptive-mesh-refinement capabilities. The objective of this study is to co-develop these codes in order to improve model fidelity and performance for each. These features will be critical for running ABL-based applications such as wind farm analysis on advanced computing architectures. To this end, we investigate the performance of NekRS and AMR-Wind on the Oak Ridge Leadership Facility supercomputers Summit, using 4 to 800 nodes (24 to 4,800 NVIDIA V100 GPUs), and Crusher, the testbed for the Frontier exascale system using 18 to 384 Graphics Compute Dies on AMD MI250X GPUs. We compare strong- and weak-scaling capabilities, linear solver performance, and time to solution. We also identify leading inhibitors to parallel scaling.

## Keywords

Exascale, Scalability, Large-Eddy Simulation

## Introduction

Atmospheric boundary layer (ABL) flows are an important part of everyday life. Aside from being a primary driver of vertical exchanges in moisture, aerosols, and atmospheric gases, the ABL affects practical aspects of life—including the transportation system, renewable energy generation, pollution dispersion, noise propagation, and transmission of electromagnetic signals. ABL flows are turbulent, and the state of the turbulence is affected by density stratification that arises in large part from surface heating and cooling. Additionally, Coriolis effects caused by planetary rotation and curvature complicate the flow. Furthermore, regional-scale weather patterns and terrain add complexity to the ABL. Significant research effort is applied to ABL flows because of their importance and complexity [Moeng \(1984\)](#); [Berg and Kelly \(2020\)](#); [Beare et al. \(2006\)](#); [Sullivan et al. \(2008\)](#); [Kosović and Curry \(2000\)](#); [Pedersen et al. \(2014\)](#); [Mirocha \(2020\)](#); [Churchfield and Moriarty \(2020\)](#). This work focuses on numerical computation of ABL flows using large eddy simulation (LES), where the governing physics equations are solved in filtered form such that the larger, energy-containing eddies are directly resolved, and the remaining “subgrid-scale” (SGS) turbulence is modeled. LES was born out of ABL research roughly five decades ago [Lilly \(1962\)](#); [Smagorinsky \(1963\)](#), and continues to evolve and improve.

Wind energy is a prime example of an application driven by the ABL. Generation of electrical energy from farms of wind turbines at night in the stable ABL is a particularly interesting situation. The winds tend to be stronger, so generation is higher. With decreased turbulence, wind turbine wakes persist for longer distances, significantly affecting wind farm efficiency and fatigue loads on waked wind turbines. With this example in mind, researchers

wish to increase grid resolution to reduce reliance on the SGS turbulence model, but they also wish to increase the overall domain size to encompass the wind farm, which commonly extends many kilometers horizontally. Increased domain size is desirable in many other applications besides wind energy. For example, LES can be used to study deep convection, which happens over a large geographical extent many kilometers into the atmosphere, and there is a push toward LES of regional-scale weather.

High-fidelity LES of the turbulent ABL is dependent on massively parallel high-performance computing (HPC). HPC architectures are evolving from traditional homogeneous x86-CPU-based computing. For example, the world’s second-fastest computer (as of June 2022), the Supercomputer Fugaku at the RIKEN Center for Computational Science [Fugaku](#), is built around Fujitsu’s custom ARM A64FX processor and does not use a GPU. Alternatively, the U.S.

<sup>1</sup>Mathematics and Computer Science, Argonne National Laboratory, Lemont, USA

<sup>2</sup>Computational Science Center, National Renewable Energy Laboratory, Golden, USA

<sup>3</sup>Mechanical Engineering, Aristotle University of Thessaloniki, Thessaloniki, Greece

<sup>4</sup>National Wind Technology Center, National Renewable Energy Laboratory, Golden, USA

<sup>5</sup>Computer Science, University of Illinois Urbana-Champaign, Urbana, USA

<sup>6</sup> Mechanical Science & Engineering, University of Illinois Urbana-Champaign, Urbana, USA

## Corresponding author:

Misun Min, Mathematics and Computer Science, Argonne National Laboratory, Lemont, USA

Email: [mmin@mcs.anl.gov](mailto:mmin@mcs.anl.gov)

Department of Energy (DOE) has embraced a hybrid CPU-GPU approach for its leadership-class computing. Summit [Summit](#), the world’s fourth-fastest computer, has nodes that house two IBM POWER9 CPUs (each with 22 cores) and six Nvidia V100 GPUs and is capable of  $200 \times 10^{15}$  floating-point operations per second (FLOPS). Similarly, DOE’s first exascale-class supercomputers, i.e., those capable of at least  $10^{18}$  FLOPS, will be a hybrid CPU-GPU based systems. Frontier, the world’s first exascale class supercomputer at the Oak Ridge Leadership Computing facility, has nodes that house one AMD CPU and 4 AMD MI250X GPUs [Frontier](#).

As described in a 2015 DOE workshop report [Sprague et al. \(2017\)](#), the transition to exascale computing brings many opportunities in computational fluid dynamics (CFD), as well as significant challenges. Two of the grand challenge opportunities described in that workshop report are relevant to this paper: the simulation of *boundary layer turbulence over large areas* and the simulation of *an entire wind farm under realistic atmospheric flow conditions*. The transition to GPU-accelerated computing is significant for those performing CFD for numerical weather forecasting or for LES of ABL flows. While hybrid CPU-GPU processing potentially enables dramatically faster computing (at low power), legacy CPU-based codes need significant overhauls or rewrites to run effectively in a CPU-GPU environment [Sprague et al. \(2017\)](#); [Robinson and Sprague \(2020\)](#).

Several groups have introduced CFD codes for LES of atmospheric flows with an emphasis on GPU calculations. While early efforts in weather forecasting on GPUs focused at  $O(100)$  m resolution (see, e.g., [Schalkwijk et al. \(2015\)](#)), more recent efforts have performed high-fidelity GPU-based LES on  $O(1)$  m grid sizes. Van Heerwaarden et al. [Van Heerwaarden et al. \(2017\)](#) introduced the MicroHH 1.0 incompressible-flow solver directed at atmospheric flow; the solver is based on finite-difference spatial discretization and a split-operator time integration. The authors showed that for problem sizes that fit, a single GPU had performance similar to that of 32 CPU cores. Sauer and Muñoz-Esparza [Sauer and Muñoz-Esparza \(2020\)](#) introduced the FastEddy LES model that was created for CPU and GPU systems. FastEddy solves the fully compressible Navier–Stokes equations using finite-difference spatial discretization and explicit Runge–Kutta time integration. The authors showed excellent scaling on up to 32 GPUs and argued that one GPU provides performance similar to that of 256 CPU cores. Recent high-order incompressible flow codes using fast tensor-product operator evaluation include ExaDG [Arndt et al. \(2020\)](#) and SPECHT\_FS [Huismann et al. \(2019\)](#) and deal.ii [Krank et al. \(2017\)](#). ExaDG and deal.ii use a discontinuous Galerkin formulation, whereas SPECHT\_FS uses a continuous Galerkin formulation similar to that in Nek5000/RS.

In this paper we examine LES modeling approaches and computational performance of two open-source, incompressible-flow, GPU-oriented CFD codes that employ fundamentally different spatial discretization and data structures. The first is NekRS [NekRS; Fischer et al. \(2021a, 2020\)](#), which is an updated version of the Nek5000

code [Nek5000](#). Nek5000/RS is a high-order, unstructured-grid, spectral-finite-element CFD code. The second is AMR-Wind [AMR-Wind](#), which is part of the ExaWind simulation suite [Sprague et al. \(2020\)](#). AMR-Wind is a block-structured, second-order, finite-volume-method CFD code with adaptive mesh refinement (AMR) capabilities and is built on the AMReX library, a software framework for massively parallel, block-structured applications [AMReX-Codes](#). Both of these codes are part of the U.S. DOE Exascale Computing Project, which is supporting the development of GPU-ready applications for exascale-class supercomputers [ECPAlexander et al. \(2020\)](#).

We compare NekRS and AMR-Wind predictions and performance on the well-known GEWEX (Global Energy and Water Cycle Experiment) Atmospheric Boundary Layer Study (GABLS) stably stratified benchmark LES case [Beare et al. \(2006\)](#), which is illustrated in Fig. 1. The flow comprises a quiescent mean flow above  $\approx 200$  m (going to the right and into the page in Fig. 1) with a sheared turbulent boundary layer (going to the right and out of the page) over the 0–200 m vertical range. The flow is coupled with thermal buoyancy effects. The computational domain is  $400 \text{ m} \times 400 \text{ m} \times 400 \text{ m}$  and doubly periodic in the streamwise ( $x$ ) and cross-flow ( $y$ ) directions. Potential temperature distributions at Reynolds number  $Re = 50M$  and  $t=6$  hours are illustrated in Fig. 2 along with profiles in Fig. 3.

In addition to investigating these codes’ ability to represent ABL physics, an objective of this study is to co-develop these codes in order to improve model fidelity and performance, features that will be critical for running ABL-based applications such as wind farm analysis on advanced computing architectures. By careful cross-comparison, both codes have made significant advances. This article focuses on performance. A separate article addresses subgrid-scale modeling for LES of the ABL. Here we investigate the scalability of NekRS and AMR-Wind on the Oak Ridge Leadership Computing Facility supercomputer Summit, using 4 to 800 nodes (24 to 4,800 NVIDIA V100 GPUs). We provide iteration counts, average-time per step, and the real-time ratio (ratio of wall-clock time to physical time), as well as detailed performance metrics. We additionally include a limited set of timing data for the two codes on Crusher, using up to 384 Graphics Compute Dies (GCDs) on AMD MI250X GPUs (one MPI rank per GCD).

The paper is organized as follows. Section II describes the codes and gives an overview of the numerical approaches used. Section III discusses the numerical setup of the simulations. Section IV provides studies comparing the codes’ performance and scaling. Section V presents a brief summary.

## Description of Codes

The numerical results are based on LES, which requires enhanced dissipation to provide an energy drain at the grid scale. Consequently, the incompressible Navier–Stokes (NS) and potential temperature equations are solved in a *spatially filtered* resolved-scale formulation, expressed in

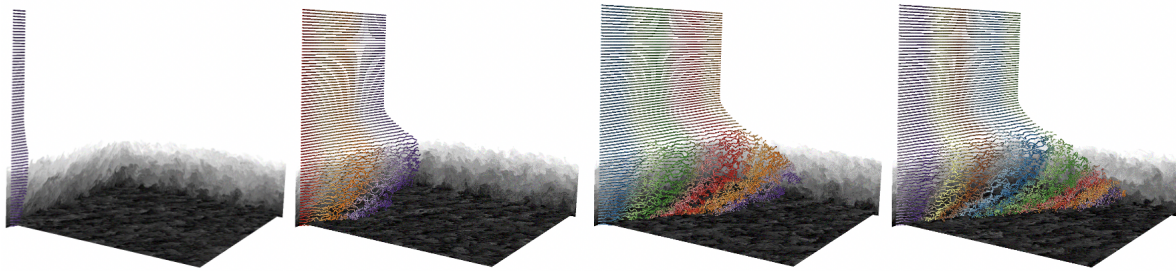


**Figure 1.** Illustration for an atmospheric boundary layer simulation with tracer particles for the GABLS benchmark problem. (Simulation by N. Lindquist [Lindquist et al. \(2021\)](#).)

nondimensional form as

$$\frac{\partial \bar{u}_i}{\partial t} + \bar{u}_j \frac{\partial \bar{u}_i}{\partial x_j} = -\frac{1}{\bar{\rho}} \frac{\partial \bar{p}}{\partial x_i} - \frac{\partial \tau_{ij}}{\partial x_j} + f_i - \frac{\theta'}{\theta_0} g_i, \quad (1)$$

$$\frac{\partial \bar{u}_j}{\partial x_j} = 0, \quad (2)$$

$$\frac{\partial \bar{\theta}}{\partial t} + \bar{u}_j \frac{\partial \bar{\theta}}{\partial x_j} = -\frac{\partial \tau_{\theta j}}{\partial x_j}, \quad (3)$$

where an overbar denotes the LES filtering operation such that  $\bar{u}_i$  is the  $i$ th component of the resolved-scale velocity vector,  $\bar{\rho}$  is the density,  $\bar{p}$  is the pressure,  $g_i$  is the gravity acceleration vector, and  $\bar{\theta}$  is the potential temperature in the resolved scale. The scalar  $\theta'/\theta_0$  that dictates the sign and strength of the buoyancy force is obtained from

$$\frac{\theta'}{\theta_0} = \frac{\bar{\theta} - \theta_0}{\theta_0}, \quad (4)$$

where  $\theta_0$  is the reference potential temperature and  $f_i$  includes the Coriolis acceleration. In addition,  $\tau_{ij}$  and  $\tau_{\theta j}$  are the stress tensors in the momentum and energy equations, respectively, which include (and are dominated by) SGS modeling terms

$$\tau_{ij} = -\frac{2}{Re} S_{ij} + \tau_{ij}^{sgs} = -\frac{1}{Re} \left( \frac{\partial \bar{u}_i}{\partial x_j} + \frac{\partial \bar{u}_j}{\partial x_i} \right) + \tau_{ij}^{sgs}, \quad (5)$$

and

$$\tau_{\theta j} = -\frac{1}{Pe} \frac{\partial \bar{\theta}}{\partial x_j} + \tau_{\theta j}^{sgs}, \quad (6)$$

where  $Re$  is the Reynolds number,  $Pe$  is the Peclet number,  $S_{ij}$  is the resolved-scale strain-rate tensor and  $\tau_{ij}^{sgs}$  and  $\tau_{\theta j}^{sgs}$  are the subgrid-scale stress tensors.

The SGS modeling in Nek5000/RS is based on [Sullivan et al. \(1994\)](#), where the SGS stress tensors  $\tau_{ij}^{sgs}$  and  $\tau_{\theta j}^{sgs}$  are expressed in terms of a non-isotropic, mean-field eddy viscosity (MFEV) obtained by the horizontally averaged mean strain rate, and an isotropic, fluctuating part. The SGS model of [Sullivan et al. \(1994\)](#) is based on the following expression:

$$\tau_{ij}^{sgs} = -2\nu_t \gamma S_{ij} - 2\nu_T \langle S_{ij} \rangle, \quad (7)$$

where the angle brackets  $\langle \rangle$  denote averaging over the homogeneous directions and  $\nu_T$  is an average eddy viscosity that is expressed in terms of mean flow quantities. In Eq. (7)  $\gamma$  is an ‘‘isotropy factor,’’ which accounts for variability

in the SGS constants due to anisotropy of the mean flow. In [Sullivan et al. \(1994\)](#), the fluctuating eddy viscosity,  $\nu_t$ , is obtained by using an eddy viscosity model based on the SGS turbulent kinetic energy equation, in which the shear production term is computed from the fluctuating velocities as suggested by [Schumann \(1975a\)](#).

Here, the fluctuating (isotropic) part is taken into account through the use of either a high-pass filter (HPF) [Stolz et al. \(2005\)](#) or a Smagorinsky (SMG) model based on the fluctuating strain rate. For the former model, which is not eddy-viscosity based,  $\nu_t$  in Eq. (7) is by definition equal to zero. On the other hand, the expression for  $\nu_T$  is derived so that the law-of-the-wall behavior can be recovered in the absence of any resolved turbulence.

The SGS modeling in AMR-Wind is based on [Smagorinsky \(1963\)](#), where a single partial differential equation for subgrid-scale kinetic energy is solved, and from that a subgrid-scale eddy viscosity is computed. The Boussinesq eddy viscosity hypothesis is then invoked to obtain the subgrid-scale stress tensor and heat flux vector.

In the following subsections we discuss the details of the numerical approaches of Nek5000/RS and AMR-Wind. For simplicity, we use  $u_i$ ,  $p$ , and  $\theta$ , dropping the overbar notation from  $\bar{u}_i$ ,  $\bar{p}$ , and  $\bar{\theta}$  in the remaining sections.

### Nek5000/RS

Nek5000 [Nek5000](#) is a spectral element code that is used for a wide range of thermal-fluids applications. It employs high-order spectral elements [Patera \(1984\)](#) in which the solution, data, and test functions are represented as *locally structured*  $N$ th-order tensor-product polynomials on a set of  $E$  *globally unstructured* curvilinear hexahedral brick elements. The approach yields two principal benefits. First, for smooth functions such as solutions to the incompressible NS equations, high-order polynomial expansions exhibit rapid convergence with approximation order, often yielding a significant reduction in the number of unknowns ( $n \approx EN^3$ ) required to reach engineering tolerances. Second, the locally structured forms permit local lexicographical ordering with minimal indirect addressing and, crucially, the use of tensor-product sum factorization to yield low  $O(n)$  storage costs and  $O(nN)$  work complexities [Orszag \(1980\)](#).

NekRS [Fischer et al. \(2021a\)](#) is a GPU-accelerated version of Nek5000 that is targeting high performance on forthcoming exascale platforms. For performance portability, NekRS is written in C++/OCCTA [Medina et al. \(2014\)](#).

Several key kernels are based on highly tuned OCCA kernels coming from the development work of Warburton and co-workers in the libParanumal library [Chalmers et al. \(2020\)](#). Specific attention in NekRS has been given to ensure scalability to  $P = 10^4$ – $10^5$  ranks and beyond [Fischer et al. \(2021b\)](#). NekRS retains access to the standard Nek5000 interface, which allows users to leverage existing user-specific source code such as statistical analysis tools for turbulence.

Time integration in Nek5000/RS is based on a semi-implicit splitting scheme using  $k$ th-order backward differences (BDF $k$ ) to approximate the time derivative coupled with implicit treatment of the viscous and pressure terms and  $k$ th-order extrapolation (EXT $k$ ) for the remaining advection and forcing terms. This approach leads to independent elliptic subproblems comprising a Poisson equation for the pressure, a coupled system of Helmholtz equations for the three velocity components, and an additional Helmholtz equation for the potential temperature. The pressure Poisson equation is obtained by taking the divergence of the momentum equation and forcing  $\frac{\partial u_i^n}{\partial x_i} = 0$  at time  $t^n = n\Delta t$ . The velocity and temperature Helmholtz equations are obtained once  $p^n$  is known:

$$-\frac{\partial^2}{\partial x_j \partial x_j} p^n = q^n, \quad (8)$$

$$\frac{\beta_0}{\Delta t} u_i^n - \frac{\partial}{\partial x_j} \left( \frac{1}{Re} + \gamma \nu_t \right) 2S_{ij}^n = -\frac{\partial}{\partial x_i} p^n + r_i^n \quad (9)$$

$$\left[ \frac{\beta_0}{\Delta t} - \frac{\partial}{\partial x_j} \left( \frac{1}{Pe} + \gamma \nu_t \right) \frac{\partial}{\partial x_j} \right] \theta^n = s^n, \quad (10)$$

where  $\beta_0$  is an order-unity constant associated with BDF $k$  [Fischer et al. \(2017\)](#);  $S_{ij}$  is the resolved-scale strain-rate tensor as described in (5); and  $q^n$ ,  $r_i^n$ , and  $s^n$  represent the sum of the values from the previous timesteps for the contributions from BDF $k$  and EXT $k$ . Also included in  $r_i^n$  and  $s^n$  are eddy diffusivity terms coming from the mean-field eddy diffusivity mentioned above. The fully coupled system of Helmholtz equations for the three velocity components (9) is used only when the fluctuating (isotropic) part of the SGS stress tensor is modeled using an SMG model based on the fluctuating strain rate. When this part is modeled through the use of a high-pass filter (HPF) [Stolz et al. \(2005\)](#), the resulting Helmholtz equations for the three velocity components are not coupled.

With the given time-splitting, we recast (8)–(10) into weak form and derive the spatial discretization by restricting the trial and test spaces to be in the finite-dimensional space spanned by the spectral element basis. The discretization leads to a sequence of symmetric positive definite linear systems for pressure, velocity, and temperature. Velocity and temperature are diagonally dominant and readily addressed with Jacobi-precondition conjugate gradient iteration. The pressure Poisson solve is treated with GMRES using  $p$ -multigrid as a preconditioner. Details of the formulation can be found in [Fischer and Lottes \(2004\)](#); [Fischer et al. \(2017\)](#); [Phillips et al. \(2022\)](#).

NekRS supports several features to accelerate performance, including overlapped communication and computation during operator evaluation, which yields a 10–15% performance gain for NS simulations; FP32 local-operator

inversion and residual evaluation for the Chebyshev-accelerated Schwarz-based  $p$ -multigrid; and projection of the velocity and pressure solutions onto the space of prior solutions to generate an initial guess, which can yield a 1.5–2-fold NS performance gain [Fischer \(1998\)](#). On the NVIDIA A100, the OCCA-based kernels are close to the bandwidth-limited roofline and are sustaining 2.1–2.2 TFLOPS (FP64) for the Poisson operator, and 3.1–3.8 TFLOPS (FP64) for the advection operator. In the pressure preconditioner, the forward Poisson operator on the coarser multigrid levels realizes 2.5–3.9 TFLOPS (FP32) and the Schwarz smoother sustains 2.5–5.1 TFLOPS (FP32). (The lower values are for smaller values of  $N$  that are used in the  $p$ -multigrid V-cycle.) Comparable values are realized on the NVIDIA V100s on Summit, save that they are  $\approx 1.5$  times lower than those on the A100. Sustained flop rates for the full NS solver are  $\approx 470$  GFLOPS per V100 on Summit, as discussed in Section .

### AMR-Wind

AMR-Wind [AMR-Wind](#) is a spatially and temporally second-order accurate finite-volume code. Important aspects of the discretization are discussed below; for more details readers can see [Almgren et al. \(1998\)](#) since the discretization is similar to the incompressible-flow solver IAMR [IAMR](#). Velocity, scalar quantities, and gradients of pressure are located at cell centers, whereas pressure is located at nodes. Partial staggering combined with an approximate projection method yields linear systems that are well studied, have small-bandwidth stencils, and can be efficiently solved with standard techniques such as geometric multigrid. These discretization choices give a well-balanced mix of both efficiency and accuracy. In addition to the spatial staggering there is also staggering in time similar to a Crank–Nicolson formulation. The time discretization is

$$\begin{aligned} \frac{c_k^{n+1} - c_k^n}{\Delta t} + \left[ \frac{\partial c_k u_j}{\partial x_j} \right]^{n+1/2} &= \frac{1}{\rho^{n+1/2}} \frac{\partial q_{kj}^{n+1}}{\partial x_j} + G_k^{n+1/2}, \\ \frac{u_i^* - u_i^n}{\Delta t} + \left[ \frac{\partial u_i u_j}{\partial x_j} \right]^{n+1/2} &= \frac{1}{\rho^{n+1/2}} \left( \frac{\partial \tau_{ij}^{n+1}}{\partial x_j} - \frac{\partial p^{n-1/2}}{\partial x_i} \right) + F_i^{n+1/2}, \end{aligned} \quad (11)$$

$$(12)$$

where  $c$  indicates a scalar quantity and  $u$  denotes velocity. The index  $n$  represents a time step, the index  $i$  runs over the three momentum equations, the index  $k$  runs over the scalar equations, and the repeated index  $j$  indicates summation.  $F_i^{n+1/2}$  and  $G_k^{n+1/2}$  are source terms and are evaluated at time step  $n + 1/2$ .  $\rho$  is density, which in these simulations is constant in time and space, but we leave the time level to show at what point in time density is evaluated if the code is run in variable-density mode.

The advection term is formed by extrapolating in time by using a Godunov method [Almgren et al. \(1998\)](#). Specifically, the velocity is first extrapolated in space (to the faces) and in time to  $n + 1/2$  in a predictor step. MAC projection [Bell](#)

et al. (1991) is applied to ensure that the face velocities are divergence free, which takes the form

$$P^{\text{MAC}}(u_i^f) = u_i^f - \frac{1}{\rho^n} \left( \frac{\partial \psi}{\partial x_i} \right),$$

where  $u_i^f$  represents a face velocity and  $\psi$  is a Lagrange multiplier located on the cells. Setting the divergence equal to zero forms a variable coefficient Poisson equation:

$$\frac{\partial}{\partial x_j} \left( \frac{1}{\rho^n} \frac{\partial \psi}{\partial x_j} \right) = \frac{\partial u_j^f}{\partial x_j}.$$

The Poisson equation is discretized by using a cell-centered seven-point stencil in 3D, which is efficiently solved by using multilevel multigrid as a linear solver Zhang et al. (2019). Once the velocity on the faces is divergence free, the advection terms are formed. Options for discretizing these advection terms include Godunov PLM Van Leer (1977), PPM Colella and Woodward (1984), and WENO-Z Motheau and Wakefield (2020). The Godunov schemes are high-order accurate and use an extended stencil. The scalar equations (e.g., potential temperature) are advanced one at a time by solving a Helmholtz problem. This Helmholtz problem is discretized by using a cell-centered finite-difference method forming a 7-point stencil in 3D Almgren et al. (1998). The momentum equations are saved for last to allow the source terms to be evaluated at  $n+1/2$  by using the previously updated scalar equations. A good example is the Boussinesq buoyancy term, which adds a source term at time step  $n+1/2$  to the momentum equation. The Boussinesq buoyancy term is a function of the already advanced potential temperature, which is averaged to time  $t^{n+1/2} = (n+1/2)\Delta t$ . The scalar equations and momentum equations can be solved by using geometric multigrid or, if diagonally dominant enough, a Krylov method such as `bicgstab` (biconjugate gradient stabilized) is sufficient. In this work, because of the small time step, we use only `bicgstab` in all of the Helmholtz solves.

The intermediate velocity  $u_i^*$  is advanced by solving a Helmholtz problem in tensor form. However, this velocity vector  $u_i^*$  is not guaranteed to be divergence free. An approximate projection method is used to solve for the velocity at time  $t^{n+1} = (n+1)\Delta t$ :

$$u^{n+1} = P(u_i^*), \quad (13)$$

where the nodal projection  $P$  is defined to be

$$P(u_i^*) = u_i^* + \frac{\Delta t}{\rho^{n+1/2}} \left( \frac{\partial p^{n-1/2}}{\partial x_i} - \frac{\partial \phi}{\partial x_i} \right). \quad (14)$$

This approximate projection is different from the algorithm in Almgren et al. (1998) and more similar to the projection in Almgren et al. (2000) labeled version 2. Taking the divergence of (14) and setting it equal to zero, we have

$$\frac{\partial}{\partial x_j} \left( \frac{\Delta t}{\rho^{n+1/2}} \frac{\partial \phi}{\partial x_j} \right) = \frac{\partial}{\partial x_j} \left( u_j^* + \frac{\Delta t}{\rho^{n+1/2}} \frac{\partial p^{n-1/2}}{\partial x_j} \right), \quad (15)$$

where  $\phi$  is a Lagrange multiplier related to the pressure field and solved on the nodes. To solve the nodal projection

in (15), a variational form is used, which leads to a 27-point stencil Almgren et al. (1998). The right-hand side of (15) is formed by taking finite differences across cells and averaging them to each node. Each node has four contributions in each coordinate direction. Once the solution  $\phi$  is obtained, the velocity is updated by using (14), and the pressure and its gradient are updated by using

$$p^{n+1/2} \leftarrow \phi, \quad \frac{\partial p^{n+1/2}}{\partial x_i} \leftarrow \frac{\partial \phi}{\partial x_i}.$$

The gradient  $\partial \phi / \partial x_i$  is approximated by taking finite differences of  $\phi$  along edges and averaging each edge to the cell center. For each coordinate direction four edges contribute to the value at the cell center.

## Simulations

We consider a stable ABL in which the ground temperature (at  $z = 0$ ) is cooler than the air temperature and where the ground temperature continues to cool over the duration of the simulation. Here we give full details of the numerical setup. The simulation domain is  $\Omega = L_x \times L_y \times L_z = 400 \text{ m} \times 400 \text{ m} \times 400 \text{ m}$ , with  $x$  the streamwise direction,  $y$  the spanwise direction, and  $z$  the vertical direction. Simulations are initialized (at  $t = 0$ ) with constant velocity in the streamwise direction equal to geostrophic wind speed of  $U = 8 \text{ m/s}$ . The initial potential temperature is 265 K in  $0 \leq z \leq 100 \text{ m}$  and linearly increased at a rate of 0.01 K/m in  $100 \text{ m} \leq z \leq 400 \text{ m}$ . The reference potential temperature is 263.5 K. The Reynolds number is  $Re = UL_b/\nu$ , where  $L_b = 100 \text{ m}$  is the thickness of the initial thermal boundary layer and  $\nu$  is the molecular viscosity. An initial perturbation is added to the temperature with an amplitude of 0.1 K on the potential temperature field for  $0 \leq z \leq 50 \text{ m}$ .

Periodic boundary conditions (BCs) are used in the streamwise and spanwise directions. At the top boundary, ( $z = 400 \text{ m}$ ), a stress-free, rigid lid is applied for momentum, and the heat flux for the energy equation is set consistent with the 0.01 K/m temperature gradient initially prescribed in the upper region of the flow. At the bottom boundary, we perform simulations with impenetrable traction BCs for the velocity where the specified shear stress comes from Monin–Obukhov similarity theory Monin and Obukhov (1954). For the energy equation, a heat flux is applied that is derived from the same theory and a specified potential temperature difference between the flow at a height,  $z_1$ , and the surface. The surface temperature is from the GABLS specification following the rule  $\theta_b(t) = 265 - 0.25t$ , where  $t$  is in hours. Because the boundary conditions are periodic (lateral), or the mass flow rate through the boundaries is zero (top and bottom), pressure boundary conditions are not needed.

In Nek5000/RS, the implementation of the traction BCs for the horizontal velocity components is performed in the context of the log-law for which we follow the approach of Grotjans and Menter (1998) and Kuzmin et al. (2007), which is appropriate for finite element methods based on a weighted residual formulation. The traction BCs imposed on the tangential velocity are based on the horizontally averaged slip velocity that develops at the boundary and the law of the wall and is effected through the use of the mean-field eddy viscosity model of Sullivan et al. (1994). The approach

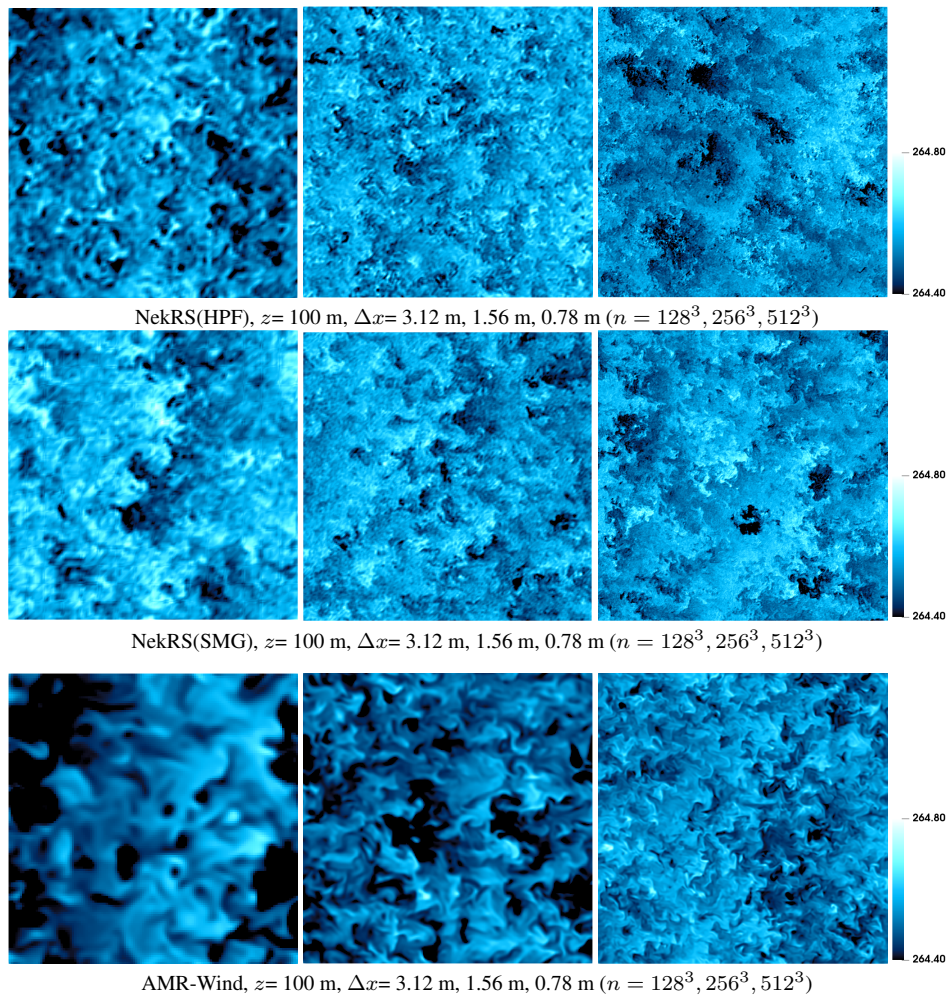


**Figure 2.** NekRS(HPF, SMG) and AMR-Wind at three grid-refinement levels for potential temperature at time 6 h.

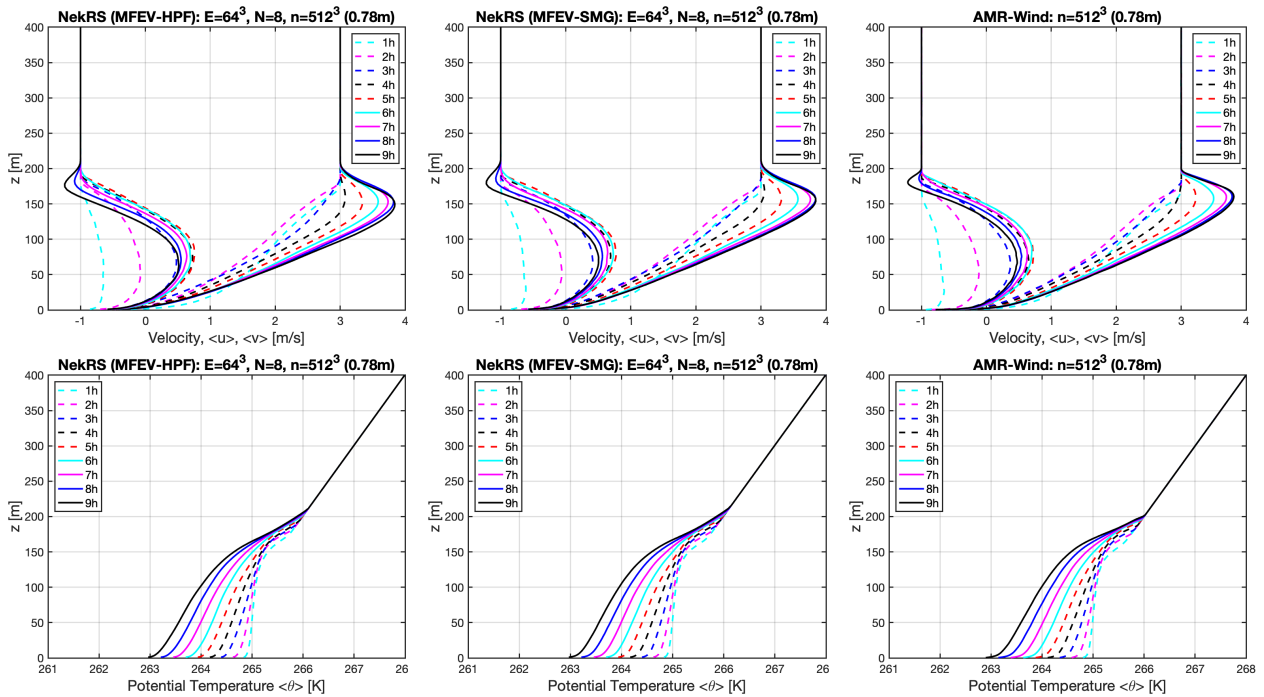


**Figure 3.** NekRS (HPF, SMG) and AMR-Wind: velocity magnitude and potential temperature at each hour, 1 h, 2 h,...,9 h.

originally used by [Schumann \(1975b\)](#) is used to convert the horizontally averaged traction to local values based on the local slip velocity in each of the horizontal directions.

In AMR-Wind, the periodic BCs in the  $x$  and  $y$  directions and the slip boundary on the top wall are applied. On the bottom wall, Dirichlet BCs in the normal direction and inhomogeneous Neumann BCs in the  $x$  and  $y$  directions are applied. The inhomogeneous Neumann BC is set using the expression for  $\tau$ , the total wall shear stress, and  $q$ , the total wall heat flux, in (16). The stresses are specified at the terrain boundary following Moeng [Moeng \(1984\)](#). The wall stress vector is defined as

$$\tau_{i3} = \frac{\bar{u}_i s + \bar{s} (u_i - \bar{u}_i)}{\bar{s}^2} u_\tau^2, \quad (16)$$

where  $u_i$  is the velocity at the first cell height,  $s$  is the wind speed  $s = \sqrt{u_1^2 + u_2^2}$ , and  $u_\tau$  is the friction velocity computed by using the Monin–Obukhov similarity law [Monin and Obukhov \(1954\)](#); [Etling \(1996\)](#). The overbar indicates a horizontal plane average at the first cell height. The heat flux is defined as

$$q = [(\theta - \bar{\theta}) \bar{s} + (\bar{\theta} - \theta_w) s] \frac{u_\tau \kappa}{\bar{s} \phi_h}, \quad (17)$$

where  $\theta$  is the temperature,  $\theta_w$  is the wall temperature,  $\kappa$  is the von Karman constant, and  $\phi_h$  comes from the Monin–Obukhov similarity law.

The range of scales in these simulations is evident in [Fig. 2](#), which shows variations in potential temperature on a horizontal  $x$ - $y$  slice at the height  $z = 100$  m. for resolutions  $\Delta x = 3.12$  m, 1.56 m, and 0.78 m, respectively from left to right, for the differing codes/models. For NekRS,  $\Delta x$  represents the average grid spacing given by  $400 \text{ m} / (E_* N)$ , where  $E_*$  is the number of elements in the  $x$ -,  $y$ -, or  $z$ -direction and  $N$  is the local polynomial order. The number of elements is  $E = E_*^3 = 16^3, 32^3, \text{ and } 64^3$  for the stated resolutions. The top row in [Figure 2](#) shows NekRS results using MFEV and HPF; the middle row shows NekRS results using MFEV and Smagorinsky, as described in Section ; and the bottom row shows AMR-Wind results. At a height of  $z = 100$  m, the temperature variations around the horizontally averaged value are small, between 264.40 K and 264.80 K. One can see that as the grid scale is decreased from  $\Delta x = 3.12$  m to 0.78 m, both codes capture increasingly finer scales. We remark that direct numerical simulation at the given Reynolds number,  $Re = 5 \times 10^7$ , would require  $\approx 10^{15}$  grid points, which is two orders of magnitude beyond current state of the art simulations of  $n = 18000^3$  for isotropic turbulence [Ravikumar et al. \(2019\)](#). The importance of the SGS model is that it potentially allows one to account for the effects of small-scale motions without needing to resolve all of them.

[Figure 3](#) shows profiles of the horizontally averaged streamwise,  $\langle u \rangle$ , and spanwise,  $\langle v \rangle$ , wind velocities (top) and potential temperature,  $\langle \theta \rangle$ , (bottom) at 1-hour time intervals between 1 h and 10 h for a mesh resolution of  $n = 512^3$  ( $\Delta x = 0.78$  m) for each code. The left figures show NekRS results using MFEV and HPF, the center figures show NekRS using MFEV and Smagorinsky, and the right figures show the results for AMR-Wind. As can be observed, the time evolution of the mean velocity and temperature profiles

obtained from the two codes agree well despite using very different numerical methods and subgrid-scale models. The agreement between AMR-Wind and NekRS improves when using MFEV and Smagorinsky (i.e., between the center and right figures). Specifically, the height of the low-level jet peak velocity during quasi-steady evolution in the GABLS problem (after approximately 7 h) is between 150 and 160 m, and its maximum value is between 9.5 and 9.7 m/s. An outgrowth of these comparative simulations has been a concerted effort to carefully validate and cross-check the SGS models. The improvement in the NekRS SGS model, realized by moving away from the HPF model to using the Smagorinsky model for the isotropic stress term, is a direct outcome of this collaborative effort.

## Performance

Here we compare performance and tuning for the two codes. For each case, the codes use the same spatial resolution,  $\Delta x$ , and timestep size,  $\Delta t$ . Each code uses iteration tolerances of  $10^{-4}$  and  $10^{-6}$  for the respective 2-norm residuals of the pressure-Poisson and velocity-Helmholtz problems. For purposes of timings, we use the solution at 6 hours as an initial condition in each case in order to ensure that performance studies are done over a timeframe in which the solutions have a representative turbulent flow. [Table 1](#) provides a summary of the test parameters, in physical units, that are used for the strong- and weak-scaling studies. The spectral element cases use 8th-order polynomial basis ( $N = 8$ ) with a number of gridpoints given by  $n = EN^3$ . For these cases we take  $\Delta x$  to be the average grid spacing in each direction (i.e.,  $400 \text{ m} / n^{1/3}$ ). For the weak-scale study, the domain height is fixed at 400 m while the dimensions are increased in the  $x$  and  $y$  directions as  $n$  is increased. In order to avoid initial transient behavior, the average (wall) time per step,  $t_{step}$ , in seconds is measured over steps 101–200.

### Performance Tuning and Profiling

We begin with performance optimization, profiling analysis, and CPU versus GPU comparisons.

NekRS GPU performance tuning on Summit is demonstrated in detail in [Fischer et al. \(2021a,b\)](#). The base libParanumal kernels have their origins in the work of Warburton and co-workers [Chalmers et al. \(2020\)](#); [Świrydowicz et al. \(2019\)](#); [Chalmers and Warburton \(2020\)](#); [Abdelfattah et al. \(2021\)](#). A key algorithmic component is the Chebyshev-accelerated Schwarz-based  $p$ -multigrid for the pressure solve [Phillips et al. \(2022\)](#), which is performed in 32-bit precision (e.g., as in [Fehn et al. \(2018\)](#)) to reduce injection-bandwidth pressure on the Summit network interface cards. Communication for the nearest-neighbor communication (direct-stiffness summation in the finite element or spectral element context [Deville et al. \(2002\)](#)) is overlapped with computation whenever it proves to be effective, which can yield as much as 10–15% savings in NS applications. At the strong-scale limit of  $\approx 2\text{M}$  points per GPU, there are enough points interior to each rank’s subdomain to balance out the communication overhead for the gather-scatter exchanges, at least at the fine-mesh level evaluations. For the coarser  $p$ -multigrid levels, it is not always the case that one can

Strong Scaling Test Sets				Weak Scaling Test Sets			
Domain size	Grid Points ( $n$ )	$\Delta x$ (m)	$\Delta t$ (s)	Domain size	Grid Points ( $n$ )	$\Delta x$ (m)	$\Delta t$ (s)
$[400 \text{ m}]^3$	$512 \times 512 \times 512$	0.78	.062500	$400 \text{ m} \times 400 \text{ m} \times 400 \text{ m}$	$512 \times 512 \times 512$	0.78	.0625
$[400 \text{ m}]^3$	$1024 \times 1024 \times 1024$	0.39	.031250	$800 \text{ m} \times 800 \text{ m} \times 400 \text{ m}$	$1024 \times 1024 \times 512$	0.78	.0625
$[400 \text{ m}]^3$	$2048 \times 2048 \times 2048$	0.19	.015625	$1600 \text{ m} \times 1600 \text{ m} \times 400 \text{ m}$	$2048 \times 2048 \times 512$	0.78	.0625
-	-	-	-	$3200 \text{ m} \times 3200 \text{ m} \times 400 \text{ m}$	$4096 \times 4096 \times 512$	0.78	.0625

**Table 1.** Problem setup for strong and weak scaling studies.

AMR-Wind: Performance progress with AMReX library updates						
Last 200 steps averaged from 1000-step run on 8 nodes using $n = 512^3$						
	Old Version		Intermediate Version		New Version	
	(s)	[%]	(s)	[%]	(s)	[%]
Wall time per timestep	3.3200e-01	100	2.4100e-01	100	2.2500e-01	100
Advection	2.9814e-02	8.98	2.6920e-02	11.17	2.8687e-02	12.75
MAC Projection	6.2582e-02	18.85	6.2660e-02	26.00	6.3135e-02	28.06
Pressure Solve	7.3671e-02	22.19	7.3481e-02	30.49	6.3180e-02	28.08
Velocity Solve	1.1401e-01	34.34	3.9669e-02	16.46	3.9307e-02	17.47
Scalar Solve	3.4827e-02	10.49	2.2148e-02	9.19	1.5930e-02	7.08
Fillpatch	1.5538e-02	4.68	1.4990e-02	6.22	1.5030e-02	6.68

**Table 2.** AMR-Wind performance optimization.

cover the communication with work. When initializing the communication kernels for each level of the  $p$ -multigrid solver, NekRS selects the fastest of several available communication strategies (e.g., overlapping, pack-on device or host, GPU direct or via the host), which are determined by timing tests during runtime setup. These unit tests also report the observed messaging bandwidth and thus provide insight into possible anomalous system behavior, which is useful when porting relatively new code to relatively new and unknown HPC platforms. For example, from existing logfiles, we were able to compare the observed bandwidth for several gather-scatter exchanges on NERSC’s Perlmutter platform before and after a network update from Cray’s Slingshot 10 to Slingshot 11, as shown below.

```

SS10:
pw+device MPI: 7.37e-05s / bi-bw: 54.5GB/s/rank
pw+device MPI: 5.16e-05s / bi-bw: 100.2GB/s/rank
pw+device MPI: 3.84e-05s / bi-bw: 33.6GB/s/rank
pw+host MPI: 2.46e-05s / bi-bw: 3.6GB/s/rank

SS11:
pw+device MPI: 4.38e-05s / bi-bw: 91.8GB/s/rank
pw+device MPI: 3.47e-05s / bi-bw: 148.8GB/s/rank
pw+device MPI: 2.74e-05s / bi-bw: 47.2GB/s/rank
pw+host MPI: 1.66e-05s / bi-bw: 5.4GB/s/rank

```

Here, SS10 indicates Slingshot 10, and SS11 indicates Slingshot 11, which shows about a  $1.5\times$  improvement over SS10. The listings also show which communication mode was used. We see that `pw+device`, which stands for pairwise device-to-device exchange (i.e., via GPU-direct) is used in most instances. The `pw+host`, which indicates the use of pairwise exchanges via the host, is used only in the case of many short messages, which is typically the scenario at the coarsest levels of the  $p$ -multigrid solver.

Over the course of the collaboration, AMR-Wind realized a  $1.4\times$  speedup with some improvements derived through AMReX library updates. The performance progress is demonstrated in Table 2, where the rows present a timing breakdown of a typical flow time step. Advection involves predicting and forming the advection term using Godunov PPM WENO. MAC projection is a Poisson equation linear

solve with a 7-point stencil that ensures that the face velocities are divergence free. The pressure solve is a Poisson equation linear solve with a 27-point stencil that approximately corrects the cell velocity to be divergence free at the end of the time step. Velocity and scalar solve are Helmholtz equations with a 7-point stencil, and Fillpatch performs all communication within and across processors outside of the linear solver communication. In the table, the *old version* is AMR-Wind using AMReX from April 2021. The *intermediate version* is the same source code but with improvements to the linear solver settings. In particular, the components of the momentum equations are solved separately instead of as a coupled tensor solve. The velocity and scalar (temperature) linear systems are solved by using bi-conjugate gradient iteration instead of a full geometric multigrid approach. In Table 2 we see that these optimizations reduce the velocity solve time by almost  $3\times$  (.114 s to .039 s) and the scalar solve time by  $1.5\times$  (.035 s to .022 s). The *new version* is AMR-Wind based on AMReX from 2022 with the same improved linear system settings. Here the scalar solve improves by another factor of 1.5. and the pressure solve is reduced from .0073 s to .0063 s per step.

For AMR-Wind, Table 3 more clearly indicates the elliptic solves as leading cost contributors. This cost is also reflected in Fig. 4, where the two largest contributors to run time are the pressure solve and the MAC projection onto a divergence-free space. In fact, these plots show that the requirement of two Poisson-like solves for AMR-Wind is the principal cause for discrepancy in run-time between the two codes. MAC projection is solved using geometric multigrid. While not necessary, it does provide more robustness and increases the stability of the scheme to CFL=2. If it did not require the MAC step, AMR-Wind would be faster on 4 nodes than NekRS. `pressureSolve` is a Poisson solve that is used at the end of the timestep to form an approximate divergence-free velocity at the cell center; it is a node-based 27 point stencil, and the linear system is solved using geometric multigrid. `scalarSolve` and `velocitySolve` are both Helmholtz solves that are cell-based 7 point stencils, the `scalarSolve` advances in time the potential Temperature



Nsight-Compute Profiling: CUDA Kernel Statistics					
11 nodes (66 GPUs), $n/P = 2.03M$ , $n = 512^3$ , 2000 steps					
NekRS					
Time [%]	Total Time (ms)	Instances	Average ( $\mu$ s)	Name	Remark
7.2	1438.604	3327	432.402	subCycleStrongCubatureVolumeHex3D	dealiasd vel. adv.
6.6	1320.502	8002	165.021	gatherScatterMany_doubleAdd	FP64 local gather-scatter
5.1	1017.806	8144	124.976	packBuf_doubleAdd	FP64 packing for gs
5.0	1009.247	3533	285.663	subCycleStrongCubatureVolumeHex3D	dealias scalar adv.
4.7	935.298	251	3726.289	scatterMany_double	FP64 scatter
4.4	879.495	8144	107.993	unpackBuf_doubleAdd	FP64 gather
3.3	667.776	3192	209.203	subCycleRKUpdate	RK4 vector update
2.9	577.150	850	679.000	ellipticStressPartialAxCoeffHex3D	viscous op. eval.
2.4	480.331	2788	172.285	ellipticPartialAxCoeffHex3D	pressure op. eval.
AMR-Wind					
Time [%]	Total Time (ms)	Instances	Average ( $\mu$ s)	Name	Remark
15.0	1890.142	142823	13.234	fab_to.fab	array box local copy
9.9	1256.128	12800	98.148	MLNodeLaplacian::Fsmooth	multigrid smoother
6.9	873.629	24800	35.227	amrex::Copy	multiple array box parallel copy
5.9	738.200	5600	131.821	MLABecLaplacian::Fapply	Laplacian op. eval.
4.5	564.742	43200	13.072	MLPoisson::Fsmooth	multigrid smoother
3.5	438.271	6800	64.451	MultiFab::LinComb	vector-vector addition
3.1	394.024	3200	123.132	MLABecLaplacian::normalize	normalize solution
3.0	384.391	800	480.488	godunov::compute_fluxes	advection momentum
2.9	359.910	800	449.887	godunov::compute_fluxes	advection scalar
2.7	344.575	11800	29.201	MultiFab::Xpay	vector-vector addition
2.4	303.2	29850	11.085	FabArray::setVal	set value of array box

**Table 3.** CUDA kernel statistics from NVIDIA® Nsight™ profiler using `nsys profile --stats=true -t nvtx,cuda`.

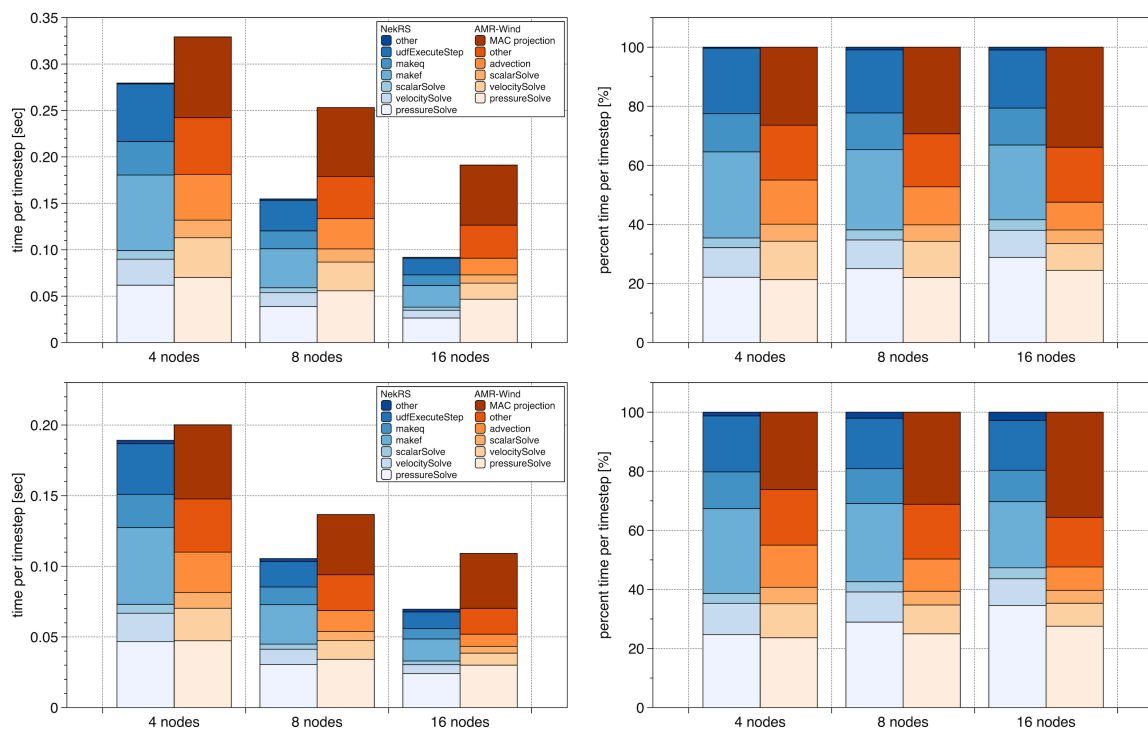


**Figure 4.** NekRS vs AMR-Wind GPU cost breakdown on Summit (top) and Crusher (bottom), using  $n = 512^3$  and 2000 steps.

equation and velocitySolve is three separate solves to advance each of the momentum equations in time. BiCG is used to solve all of the linear Helmholtz subproblems. The advection terms in the governing equations are discretized using a Godunov WENO-Z scheme to provide these terms on the cell faces at time  $t^{n+\frac{1}{2}}$ . Other function calls comprise source term calculations, boundary conditions, planar averaging, communication (excluding linear solve

communication), linear solve setup, and copying solution arrays.

For AMR-Wind on both Summit and Crusher, the time per step,  $t_{step}$ , decreases with increasing node count as each component of the timestep takes less time. Both Poisson solves, however, take a higher percentage of the time step as  $P$  is increased, which reflects the communication-intensive nature of the Poisson problem. Overall, Crusher is providing better performance than Summit. This is partly because there

Platform	Kernel	$N$	FP	GB/s	GFLOPS	KV
Summit	advSub (3)	10	64	613	3773	7
NVIDIA	advSub (1)	10	64	1137	2446	8
V100	Ax	8	64	844	1622	5
( $P=24$ )	Ax	8	64	900	1731	4
	Ax	8	64	901	1732	4
	Ax	8	32	859	3303	4
	Ax	4	64	832	975	5
	Ax	4	32	711	1667	6
	fdm	10	32	611	6210	3
	fdm	6	32	713	4422	3
Crusher	advSub (3)	10	64	491	3018	11
AMD	advSub (1)	10	64	868	1867	8
MI250X	Ax	8	64	662	1272	2
( $P=32$ )	Ax	8	64	736	1416	2
	Ax	8	64	736	1415	2
	Ax	8	32	742	2854	2
	Ax	4	64	708	830	6
	Ax	4	32	658	1543	0
	fdm	10	32	546	5551	4
	fdm	6	32	521	3234	4
Summit	Sustained		64		833	
Crusher	Sustained		64		937	

**Table 4.** NekRS runtime benchmark results associated with Fig. 4.

are more GPUs per node (8 versus 6) but also because the mesh decomposition has better load balancing for AMR-Wind. A problem size of  $512^3$  is more easily partitioned by 8 GPUs/node versus 6 GPUs/node. With 16 Crusher nodes (128 GPUs) a time per timestep of  $t_{step}=0.11$  s is achieved with AMR-Wind. Further scaling out with Summit the lowest time per timestep was 0.128 s on 128 Summit nodes (768 GPUs), as discussed below.

For NekRS, we start the GPU analysis with NVIDIA’s profiling tools. Table 3 summarizes the kernel-level metrics for the critical kernels, which are identified with NVIDIA’s Nsight Systems. At this granularity, the table indicates that the bulk of the time for NekRS is spent evaluating the dealiased advection operator (subCycleStrongCubatureVolumeHex3D) both for the velocity vectors and for the temperature. Other leading consumers are the gather-scatter operations. Largely missing from this table for NekRS is the time spent in the pressure preconditioner, which is separated across many kernels for the various levels of  $p$ -multigrid.

Each NekRS job tracks basic runtime statistics using a combination of MPI Wtime and cudaDeviceSynchronize or CUDA events. These are output every 500 time steps unless the user specifies otherwise. From these, we collect aggregate timing breakdowns, roughly following the physical substeps of advection, pressure, and viscous-thermal-updates, plus tracking of known communication bottlenecks such as the pMG coarse-grid solve for the pressure preconditioner. Figure 4 shows the cost breakdown for this type of analysis over node counts ranging from 4 to 16. At lower node counts, the bulk of the NekRS time is spent in the makef and makeq (advection) routines, which are respectively responsible for setting up the right-hand-sides for the momentum and energy equations. To allow a larger CFL, the ABL simulations use characteristics-based timestepping, which involves solving a sequence of hyperbolic subproblems on the interval  $[t^{n-2}, t^n]$  (one

for each velocity component and one for temperature) Maday et al. (1990); Patel et al. (2019). Each subproblem takes several substeps using the dealiased advection operator, which performs quadrature on a  $11 \times 11 \times 11$  grid in each element. These substeps are thus compute-intensive but not communication intensive, so they scale relatively well. velocitySolve and scalarSolve, which involve communication-free diagonal preconditioning for conjugate gradient solution of (9)–(10), show similar scaling behavior. As with AMR-Wind, we see clearly in Fig. 4 that the pressure solve not scale as well as the other components.

We remark that Fig. 4 indicates a significant amount of time is spent in udfExecuteStep. The majority of that cost results from the recently adopted mean-field eddy viscosity model (7), which requires several planar averages per time step and is currently implemented as a user-defined function. For these calculations, which have low pressure and velocity iteration counts, the frequently called planar average utility has a significant impact on runtime (about 20%). Planar averaging is typically a post-processing operation that is not performed on every step, but clearly it will need to be optimized in this LES application.

Table 4 gives a detailed breakdown of the per rank\* kernel performance for NekRS in the 4-node case of Fig. 4. The kernels are the advection subroutine (advSub), with either 3 components (velocity) or 1 (temperature); the Poisson/Helmholtz matrix-vector product (Ax) for the elliptic solves; and the fast-diagonalization method (fdm) for the Schwarz smoother Lottes and Fischer (2005). For each kernel,  $N$  indicates the polynomial order. To leading order, the amount of tensor-contraction work for each operation scales as  $CE_p(N+1)^4$  and the number of memory references as  $CE(N+1)^3$ , with  $E_p$  the number of elements on each rank and  $C \approx 12\text{--}30$  a kernel-dependent constant. FP indicates the working floating-point precision; GB/s the sustained streaming bandwidth on the device; GFLOPS the number of billions of floating-point operations per second sustained on the device for that particular kernel; and KV the kernel version identified as the fastest entry in each runtime benchmark test. The 32-bit precision kernels are used in the lower levels of  $p$ -multigrid. Because the Schwarz smoother operates on an extended domain, fdm executes on data that is extended to  $N+2$  in each direction compared with its corresponding Ax operation. The advection operation is dealiased (i.e., integration is on a finer mesh than the underlying velocity representation), so that kernel also operates on a relatively large data set. We see that the work-intensive (high- $N$ ) and 32-bit kernels achieve impressive floating-point performance, well in excess of 1 TFLOPS (incidentally, the speed of ASCI Red, the world’s fastest computer just 25 years ago). NekRS also provides a conservative estimate of the overall FP64 floating point rate per rank—here, close to 1 TFLOPS—which includes the message-passing overhead. (For this overall rate, each 32-bit operation is counted as half a flop.)

Figure 5 shows CPU and GPU strong-scaling performance for each code on Summit. The upper figures show standard

\*One rank corresponds to a single V100 on Summit or a single MI250X GCD on Crusher.

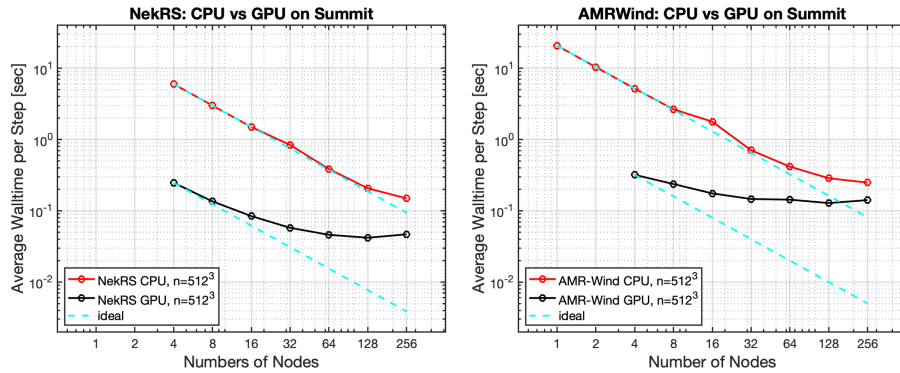


**Figure 5.** NekRS and AMR-Wind: CPU vs. GPU performance on Summit: 100 steps average from 200 step runs for  $n = 512^3$ .

time vs. node-count plots, which clearly indicate that it is easier to strong-scale on the CPU. On Summit, however, that point is moot given that one needs 128 nodes using a CPU-only configuration in order to get to the same time-per-step as using 4 nodes with 6 GPUs each (i.e., a factor of 32 difference in required node-hours to do the same work).

### Strong- and Weak-Scaling Performance

We next consider GPU-only performance on Summit using a single V100 per MPI rank. Figure 6, top, shows performance in terms of  $t_{step}$  for strong scaling as a function of the number of GPUs,  $P$ , in the left column and as a function of number of points per rank,  $n/P$ , in the center column. Weak-scaling performance is presented in the right column. The wall-time figure also shows the ideal speed-up curves scaling as  $P^{-1}$ . The lower plots show parallel efficiency,

$$P_{\text{eff}} := \frac{t_0 P_0}{t_{\text{step}} P}, \quad (18)$$

where  $P_0$  is the smallest value of  $P$  that will hold the given problem and  $t_0$  is the  $t_{step}$  value corresponding to  $P_0$ .

We see that at the lower resolution of  $n = 512^3$ , the performance of the two codes is within a factor of 2 of each other out to  $P = 78$ . From the efficiency figures we can see that both curves have dropped below 80% efficiency by that point, so a more realistic point of comparison would be at  $P = 66$  given that users would typically not run this relatively small case on  $P > 66$ . We note that  $P = 66$  corresponds to  $n/P = 2\text{M}$ , which is a typical strong-scaling limit for NekRS on current-generation GPU platforms.

The center column in Fig. 6 replots the strong-scaling information with  $n/P$  as the independent variable. Here we see a collapse of each code's strong-scale data into a single curve, particularly for NekRS. The efficiency plot, lower-center, clearly shows the  $n/P = 2\text{M}$  mark as the 80% parallel efficiency point for NekRS. The AMR-Wind wall-time curves, upper center, are not as tightly grouped, particularly for the large problem sizes on large processor counts. It is tempting to speculate that this increased cost is due to an increase in iteration count, but Tables 5 and 6 show that is not the case, since each solver requires only two iterations per timestep for each of the problems. An important feature of AMR-Wind is that it generally performs better if  $P$  is a power of 2. At the critical point of  $n/P = 2\text{M}$ ,

NekRS is only a factor of 1.6 faster than AMR-Wind for the  $n = 512^3$  case.

Figure 6, right, shows weak-scaling results for  $n/P = 2.2\text{M}$  and  $4.4\text{M}$ . For the heavily loaded cases, AMR-Wind is within a factor of 1.6 of NekRS, but this figure increases to roughly a factor of 2 for the  $2.2\text{M}$  points-per-GPU case. The weak-scale efficiency reaches 80% at around  $P = 2000$  GPUs for all the cases save the AMR-Wind case with  $n/P = 2.2\text{M}$ , which crosses the 80% mark at  $P \approx 1100$ .

Tables 5 and 6 provide a detailed breakdown of several of the key metrics for the code performance, including iteration counts ( $v_i$ ,  $p_i$ ,  $T_i$ , for the respective velocity, pressure, and temperature iterative solvers),  $t_{step}$ , parallel efficiency ( $P_{\text{eff}}$ ), and the wall-time to physical-time ratio ( $r_t$ ). This last quantity is of particular interest since it must be smaller than unity for weather modeling applications. We also note that  $P$  is denoted by `gpu` in the tables. We see from Table 5 that, for a fixed value of  $n/P$ ,  $r_t$  effectively doubles with each doubling of (linear) resolution. The reason for this increase is that the number of timesteps must also double whenever the number of points in each direction is doubled (for fixed domain size). Throughout the table, we see that roughly two iterations are required per timestep for each of the linear solvers, indicating that the preconditioners are robust with respect to mesh size, although NekRS does show some increase in iteration count in the weak-scale results.

We remark that AMR supports block-structured adaptive mesh refinement, which means that static grids do not leverage one of its main features. It is nonetheless highly performant on this problem. Moreover, AMR-Wind has a significant performance boost when the number of ranks is a power of 2, as seen in Table 5 for the  $n = 1024^3$  case for  $P = 512$  and in the  $n = 2048^3$  case for  $P = 4096$ . In the former case, the parallel efficiency jumps from 49% to 67% as  $P$  changes from 480 to 512. In the latter, it jumps from 40% for  $P = 3840$  to 51% for  $P = 4096$ . These performance gains derive from the block decompositions used in AMR-Wind, which favor block sizes (and thus, processor counts) that are powers of 2.

We close with a scaling comparison of Summit and Crusher performance for NekRS in Fig. 7. The upper figures show standard strong scaling as a function of the number of ranks on the left (one GPU or GCD per rank) and as a function of  $n/P$  on the right. The lower plots show the timing for the `makef` kernel (left), which

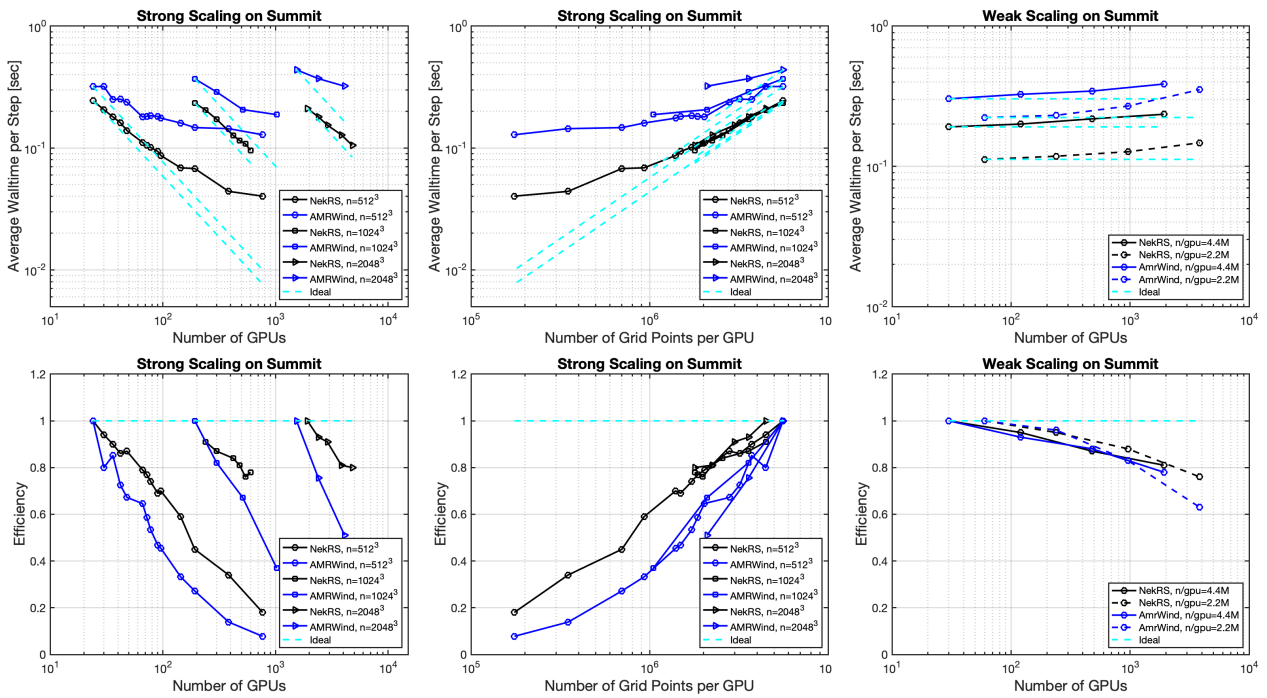


Figure 6. NekRS vs. AMR-Wind strong and weak scaling on Summit GPUs.

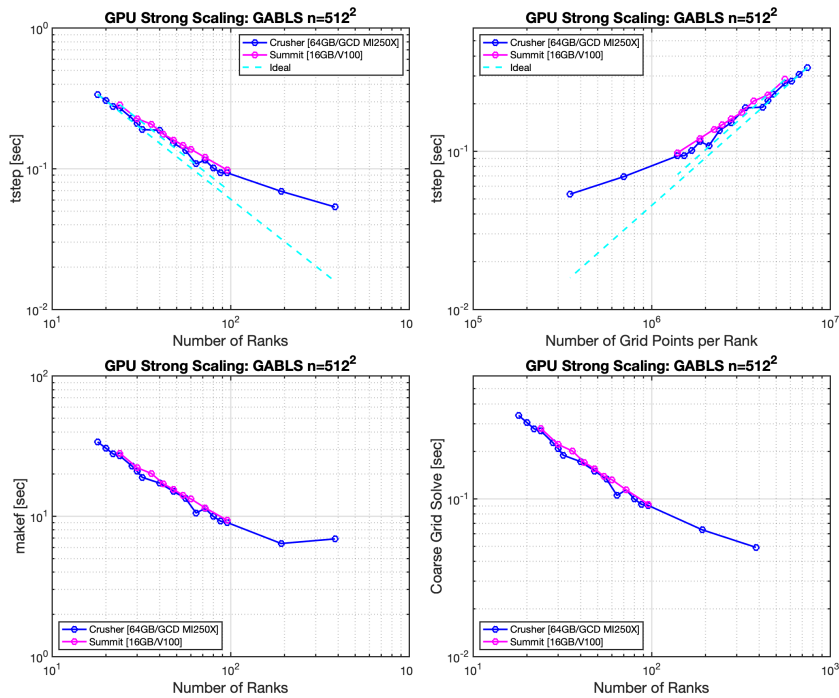


Figure 7. NekRS GPU strong-scaling comparison on Crusher and Summit.

evaluates the nonlinear advection term and does not require communication, and for the coarse-grid solve (right), which is communication dominated. The coarse-grid problem, which has roughly  $E$  degrees of freedom (with  $E = 262144$  in this case), is solved by using algebraic multigrid (hypre) on the host CPUs. The performance for these two platforms is remarkably similar.

## Conclusion

We presented profiling and timing results for two CFD codes, NekRS and AMR-Wind, applied to the GABLS atmospheric boundary layer test problem, which is of direct relevance to wind farm modeling and weather forecasting. Strong and weak scaling were demonstrated on up to  $P = 4800$  NVIDIA V100 GPUs on OLCF's Summit. For NekRS, wall-clock times of 0.11 s were observed for  $n/P = 2M$ , which is the 80% efficiency point across a range of

Strong-Scaling on Summit GPU, $n = 512^3$ , $\Delta x = 0.78$ m, $\Delta t = 6.25e-2s$ , $\Omega = [400 \text{ m} \times 400 \text{ m} \times 400 \text{ m}]$															
			NekRS						AMR-Wind						
node	gpu	$n/\text{gpu}$	$v_i$	$p_i$	$T_i$	$t_{step}$	$P_{eff}$	$r_t$	$v_i$	$p_i$	$T_i$	$t_{step}$	$P_{eff}$	$r_t$	
4	24	5.5924e+06	2	1.81	1	2.44e-01	100	3.90	2	2	2	3.19e-01	100	5.10	
8	48	2.7962e+06	2	1.82	1	1.39e-01	87	2.22	2	2	2	2.37e-01	67	3.80	
11	66	2.0336e+06	2	1.85	1	1.11e-01	79	1.78	2	2	2	1.79e-01	64	2.87	
16	96	1.3981e+06	2	1.90	1	8.66e-02	70	1.38	2	2	2	1.75e-01	45	2.80	
24	144	9.3207e+05	2	2.00	1	6.87e-02	59	1.09	2	2	2	1.60e-01	33	2.56	
32	192	6.9905e+05	2	2.00	1	6.77e-02	45	1.08	2	2	2	1.46e-01	27	2.34	
64	384	3.4953e+05	2	2.00	1	4.40e-02	34	0.70	2	2	2	1.43e-01	13	2.30	
128	768	1.7476e+05	2	2.00	1	4.02e-02	18	0.64	2	2	2	1.28e-01	7.7	2.05	
256	1536	8.7381e+04	2	2.00	1	3.60e-02	10	0.57	2	2	2	1.41e-01	3.5	2.26	
Strong-Scaling on Summit GPU, $n = 1024^3$ , $\Delta x = 0.39$ m, $\Delta t = 3.125e-2s$ , $\Omega = [400 \text{ m} \times 400 \text{ m} \times 400 \text{ m}]$															
			NekRS						AMR-Wind						
node	gpu	$n/\text{gpu}$	$v_i$	$p_i$	$T_i$	$t_{step}$	$P_{eff}$	$r_t$	$v_i$	$p_i$	$T_i$	$t_{step}$	$P_{eff}$	$r_t$	
32	192	5.5924e+06	1	1.4	1	2.34e-01	100	7.50	2	2	2	0.369	100	11.82	
40	240	4.4739e+06	1	1.3	1	2.04e-01	91	6.54	2	2	2	0.402	73	12.86	
50	300	3.5791e+06	1	1.4	1	1.72e-01	87	5.50	2	2	2	0.288	82	9.21	
70	420	2.5565e+06	1	1.4	1	1.27e-01	84	4.06	2	2	2	0.303	56	9.72	
80	480	2.2370e+06	1	1.3	1	1.15e-01	81	3.68	2	2	2	0.301	49	9.65	
86	512	2.0972e+06	-	-	-	-	-	-	2	2	2	0.206	67	6.60	
90	540	1.9884e+06	1	1.3	1	1.08e-01	76	3.47	2	2	2	0.217	60	6.95	
100	600	1.7896e+06	1	1.3	1	9.57e-02	78	3.06	2	2	2	0.219	54	7.01	
Strong-Scaling on Summit GPU, $n = 2048^3$ , $\Delta x = 0.39$ m, $\Delta t = 1.5625e-2s$ , $\Omega = [400 \text{ m} \times 400 \text{ m} \times 400 \text{ m}]$															
			NekRS						AMR-Wind						
node	gpu	$n/\text{gpu}$	$v_i$	$p_i$	$T_i$	$t_{step}$	$P_{eff}$	$r_t$	$v_i$	$p_i$	$T_i$	$t_{step}$	$P_{eff}$	$r_t$	
256	1536	5.5924e+06	-	-	-	-	-	-	2	2	2	0.437	100	34.99	
320	1920	4.4739e+06	1	1.16	1	2.10e-01	100	16.8	2	2	2	0.485	72	38.80	
400	2400	3.5791e+06	1	1.20	1	1.80e-01	93	14.4	2	2	2	0.370	76	29.62	
480	2880	2.9826e+06	1	1.22	1	1.54e-01	91	12.3	2	2	2	0.402	58	32.16	
640	3840	2.2370e+06	1	1.25	1	1.28e-01	81	10.3	2	2	2	0.440	40	35.26	
683	4096	2.0972e+06	-	-	-	-	-	-	2	2	2	0.321	51	25.69	
800	4800	1.7896e+06	1	1.18	1	1.05e-01	80	8.4	2	2	2	0.390	36	31.23	

**Table 5.** NekRS GPU vs. AMR-Wind GPU strong-scaling performance study.

Weak-Scaling on Summit GPU, $\Delta x = 0.78$ m, $\Delta t = 6.25e-2s$																
					NekRS						AMR-Wind					
node	gpu	$n$	$\Omega$	$n/\text{gpu}$	$v_i$	$p_i$	$T_i$	$t_{step}$	$P_{eff}$	$r_t$	$v_i$	$p_i$	$T_i$	$t_{step}$	$P_{eff}$	$r_t$
5	30	$512^2 \times 512$	$400 \text{ m}^2 \times 400 \text{ m}$	4.4739e+06	1	1.5	1	0.191	100	3.8	2	2	2	0.303	100	4.8
20	120	$1024^2 \times 512$	$800 \text{ m}^2 \times 400 \text{ m}$	4.4739e+06	1	1.7	1	0.200	95	4.0	2	2	2	0.326	93	5.2
80	480	$2048^2 \times 512$	$1600 \text{ m}^2 \times 400 \text{ m}$	4.4739e+06	1	1.9	1	0.218	87	3.8	2	2	2	0.344	88	5.5
320	1920	$4096^2 \times 512$	$3200 \text{ m}^2 \times 400 \text{ m}$	4.4739e+06	1	2.4	1	0.235	81	4.7	2	2	2	0.386	78	6.2
					NekRS						AMR-Wind					
node	gpu	$n$	$\Omega$	$n/\text{gpu}$	$v_i$	$p_i$	$T_i$	$t_{step}$	$P_{eff}$	$r_t$	$v_i$	$p_i$	$T_i$	$t_{step}$	$P_{eff}$	$r_t$
10	60	$512^2 \times 512$	$400 \text{ m}^2 \times 400 \text{ m}$	2.2370e+06	1	1.5	1	0.112	100	2.2	2	2	2	0.223	100	3.6
40	240	$1024^2 \times 512$	$800 \text{ m}^2 \times 400 \text{ m}$	2.2370e+06	1	1.7	1	0.118	95	2.4	2	2	2	0.231	96	3.7
160	960	$2048^2 \times 512$	$1600 \text{ m}^2 \times 400 \text{ m}$	2.2370e+06	1	2.1	1	0.127	88	2.5	2	2	2	0.269	83	4.3
640	3840	$4096^2 \times 512$	$3200 \text{ m}^2 \times 400 \text{ m}$	2.2370e+06	1	2.5	1	0.147	76	2.9	2	2	2	0.352	63	5.6

**Table 6.** NekRS GPU vs. AMR-Wind GPU weak-scaling performance study with fixed mesh density and resolution per GPU.

problem sizes. AMR-Wind was generally within a factor of 1.4–2.0 of the performance of NekRS over the range of interest. For both codes, the substep that inhibits strong scaling is the intrinsically communication-intensive pressure Poisson solve. For NekRS it was shown that a single GCD of the MI250X on Crusher is delivering performance that is comparable to a single V100 on Summit. Finally, we demonstrated that careful subgrid-scale modeling is critical to realizing comparable results. A future paper will investigate the modeling questions more deeply.

## Acknowledgments

This material is based upon work supported by the U.S. Department of Energy, Office of Science, under contract DE-AC02-06CH11357 and by the Exascale Computing Project (17-SC-20-SC). The research used resources at the Oak Ridge Leadership Computing Facility at Oak Ridge National Laboratory, which is supported by the Office of Science of the U.S. Department of Energy under Contract DE-AC05-00OR22725.

## References

Abdelfattah A, Barra V, Beams N, Bleile R, Brown J, Camier JS, Carson R, Chalmers N, Dobrev V, Dudouit Y, Fischer P, Karakus A, Kerkemeier S, Kolev T, Lan YH, Merzari E, Min

- M, Phillips M, Rathnayake T, Rieben R, Stitt T, Tomboulides A, Tomov S, Tomov V, Vargas A, Warburton T and Weiss K (2021) GPU algorithms for efficient exascale discretizations. *Parallel Comput.* 108.
- Alexander F, Almgren A, Bell J, Bhattacharjee A, Chen J, Colella P, Daniel D, DeSlippe J, Diachin L, Draeger E et al. (2020) Exascale applications: skin in the game. *Philosophical Transactions of the Royal Society A* 378(2166): 20190056.
- Almgren AS, Bell JB, Colella P, Howell LH and Welcome ML (1998) A conservative adaptive projection method for the variable density incompressible navier-stokes equations. *Journal of Computational Physics* 142(1): 1–46. DOI:10.1006/jcph.1998.5890.
- Almgren AS, Bell JB and Crutchfield WY (2000) Approximate projection methods: Part i. inviscid analysis. *SIAM Journal on Scientific Computing* 22(4): 1139–1159. DOI:10.1137/S1064827599357024. URL <https://doi.org/10.1137/S1064827599357024>.
- AMR-Wind (2020) Massively parallel, block-structured adaptive-mesh, incompressible flow solver. <https://github.com/Exawind/amr-wind>.
- AMReX-Codes (2019) Block-Structured AMR Software Framework and Applications. <https://github.com/AMReX-Codes/amrex>.
- Arndt D, Fehn N, Kanschat G, Kormann K, Kronbichler M, Munch P, Wall W and Witte J (2020) ExaDG: High-order discontinuous Galerkin for the exa-scale. In: Bungartz H, Reiz S, Uekermann B, Neumann P and Nagel W (eds.) *Software for Exascale Computing - SPPEXA 2016-2019*. Springer, pp. 189–224.
- Beare R, Macvean M, Holtslag A, Cuxart J, Esau I, Golaz JC, Jimenez M, Khairoutdinov M, Kosovic D and Lewellen et al. (2006) An intercomparison of large-eddy simulations of the stable boundary layer. *Boundary-Layer Meteorology* 118(2): 247–272.
- Bell JB, Howell LH and Colella P (1991) An efficient second-order projection method for viscous incompressible flow.
- Berg J and Kelly MC (2020) Atmospheric turbulence modelling, synthesis, and simulation. In: *Wind Energy Modeling and Simulation: Volume 1: Atmosphere and Plant*. Inst. Eng. and Tech., pp. 183–216.
- Chalmers N, Karakus A, Austin AP, Swirydowicz K and Warburton T (2020) libParanumal: a performance portable high-order finite element library. DOI:10.5281/zenodo.4004744. URL [github.com/paranumal/libparanumal](https://github.com/paranumal/libparanumal).
- Chalmers N and Warburton T (2020) Portable high-order finite element kernels I: streaming operations. *CoRR* abs/2009.10917. URL <https://arxiv.org/abs/2009.10917>.
- Churchfield M and Moriarty P (2020) Modeling and simulation of wind-farm flows. In: *Wind Energy Modeling and Simulation: Volume 1: Atmosphere and Plant*. Inst. Eng. and Tech., pp. 217–271.
- Colella P and Woodward PR (1984) The piecewise parabolic method (ppm) for gas-dynamical simulations. *Journal of Computational Physics* 54(1): 174–201. DOI: [https://doi.org/10.1016/0021-9991\(84\)90143-8](https://doi.org/10.1016/0021-9991(84)90143-8). URL <https://www.sciencedirect.com/science/article/pii/0021999184901438>.
- Deville M, Fischer P and Mund E (2002) *High-order methods for incompressible fluid flow*. Cambridge: Cambridge University Press.
- ECP (????) Exascale Computing Project. <https://www.exascaleproject.org/>.
- Etling D (1996) Modelling the vertical ABL structure. *Modelling Of Atmospheric Flow Fields* : 45.
- Fehn N, Wall W and Kronbichler M (2018) Efficiency of high-performance discontinuous Galerkin spectral element methods for under-resolved turbulent incompressible flows. *Int. J. Numer. Methods Fluids* URL <https://doi.org/10.1002/flid.4511>.
- Fischer P (1998) Projection techniques for iterative solution of  $A\bar{x} = \bar{b}$  with successive right-hand sides. *Comput. Methods Appl. Mech. Engrg.* 163: 193–204.
- Fischer P, Kerkemeier S, Min M, Lan Y, Phillips M, Rathnayake T, Merzari E, Tomboulides A, Karakus A, Chalmers N and Warburton T (2021a) NekRS, a GPU-accelerated spectral element Navier-Stokes solver. *CoRR* abs/2104.05829. URL <https://arxiv.org/abs/2104.05829>.
- Fischer P, Kerkemeier S, Min M, Lan YH, Phillips M, Rathnayake T, Merzari E, Tomboulides A, Karakus A, Chalmers N and Warburton T (2020) NekRS, a GPU-accelerated spectral element Navier–Stokes solver. *Parallel Comput.* submitted.
- Fischer P and Lottes J (2004) Hybrid Schwarz-multigrid methods for the spectral element method: Extensions to Navier-Stokes. In: Kornhuber R, Hoppe R, Périaux J, Pironneau O, Widlund O and Xu J (eds.) *Domain Decomposition Methods in Science and Engineering Series*. Springer, Berlin.
- Fischer P, Merzari E, Min M, Kerkemeier S, Lan Y, Phillips M, Rathnayake T, Novak A, Gaston D, Chalmers N and Warburton T (2021b) Highly optimized full-core reactor simulations on Summit. *arXiv preprint arXiv:2110.01716* .
- Fischer P, Schmitt M and Tomboulides A (2017) *Recent developments in spectral element simulations of moving-domain problems*, volume 79. Fields Institute Communications, Springer, pp. 213–244.
- Frontier (2022) OLCF. <https://www.olcf.ornl.gov/frontier/>.
- Fugaku (2020) RIKEN Center for Computational Science. <https://www.r-ccs.riken.jp/en/fugaku/>.
- Grotjans H and Menter F (1998) Wall functions for general application CFD codes. In: *ECCOMAS 98, Proc. 4th European Computational Fluid Dynamics Conference, John Wiley & Sons*. pp. 1112–1112.
- Huisman I, Stiller J and Fröhlich J (2019) Scaling to the stars – a linearly scaling elliptic solver for  $p$ -multigrid. *J. Comput. Phys.* 398: 108868.
- IAMR (2017) An adaptive mesh, variable-density incompressible Navier Stokes solver. <https://amrex-codes.github.io/IAMR/>.
- Kosović B and Curry JA (2000) A large eddy simulation study of a quasi-steady, stably stratified atmospheric boundary layer. *Journal of the atmospheric sciences* 57(8): 1052–1068.
- Krank B, Fehn N, Wall W and Kronbichler M (2017) A high-order semi-explicit discontinuous Galerkin solver for 3D incompressible flow with application to DNS and LES of turbulent channel flow. *J. Comput. Phys.* 348(1): 634–659. DOI:10.1016/j.jcp.2017.07.039.

- Kuzmin D, Mierka O and Turek S (2007) On the implementation of the k- $\epsilon$  turbulence model in incompressible flow solvers based on a finite element discretisation. *International Journal of Computing Science and Mathematics* 1: 193–206. DOI: 10.1504/IJCSM.2007.016531.
- Lilly DK (1962) On the numerical simulation of buoyant convection. *Tellus* 14(2): 148–172.
- Lindquist N, Min M and Fischer P (2021) Scalable interpolation on gpus for thermal fluids applications. Technical Report ANL-21/55, Argonne National Laboratory.
- Lottes JW and Fischer PF (2005) Hybrid multigrid/Schwarz algorithms for the spectral element method. *J. Sci. Comput.* 24: 45–78.
- Maday Y, Patera A and Rønquist E (1990) An operator-integration-factor splitting method for time-dependent problems: Application to incompressible fluid flow. *J. Sci. Comput.* 5: 263–292.
- Medina DS, St-Cyr A and Warburton T (2014) OCCA: A unified approach to multi-threading languages. *arXiv preprint arXiv:1403.0968*.
- Mirocha JD (2020) Mesoscale to microscale coupling for high-fidelity wind plant simulation. In: *Wind Energy Modeling and Simulation: Volume 1: Atmosphere and Plant*. Inst. Eng. and Tech., pp. 117–181.
- Moeng CH (1984) A large-eddy-simulation model for the study of planetary boundary-layer turbulence. *Journal of the Atmospheric Sciences* 41(13): 2052–2062.
- Monin AS and Obukhov AM (1954) Basic laws of turbulent mixing in the surface layer of the atmosphere. *Tr. Akad. Nauk. SSSR Geophys. Inst.* 24(151): 163–187.
- Motheau E and Wakefield J (2020) Investigation of finite-volume methods to capture shocks and turbulence spectra in compressible flows. *Communications in Applied Mathematics and Computational Science* 15(1): 1–36.
- Nek5000 (1989) Open source spectral element CFD solver.
- NekRS (2019) GPU-accelerated Navier Stokes solver. <https://github.com/Nek5000/nekRS>.
- Orszag S (1980) Spectral methods for problems in complex geometry. *J. Comput. Phys.* 37: 70–92.
- Patel S, Fischer P, Min M and Tomboulides A (2019) A characteristic-based, spectral element method for moving-domain problems. *J. Sci. Comp.* 79: 564–592.
- Patera A (1984) A spectral element method for fluid dynamics: laminar flow in a channel expansion. *J. Comput. Phys.* 54: 468–488.
- Pedersen JG, Gryning SE and Kelly M (2014) On the structure and adjustment of inversion-capped neutral atmospheric boundary-layer flows: Large-eddy simulation study. *Boundary-Layer Meteorology* 153(1): 43–62. DOI:10.1007/s10546-014-9937-z. URL <https://doi.org/10.1007/s10546-014-9937-z>.
- Phillips M, Kerkemeier S and Fischer P (2022) Tuning spectral element preconditioners for parallel scalability on GPUs. In: *Proc. of the 2022 SIAM Conf. on Par. Proc. for Sci. Comp.* SIAM, pp. 37–48.
- Ravikumar K, Appelhans D and Yeung P (2019) Acceleration of extreme scale pseudo-spectral simulations of turbulence using asynchronism. In: *Proc. of the Int. Conf. for High Perf. Comp., Net., Storage and Analysis*. pp. 8 (1–22). URL <https://doi.org/10.1145/3295500.3356209>.
- Robinson MC and Sprague MA (2020) Looking forward: The promise and challenge of exascale computing. In: *Wind Energy Modeling and Simulation: Volume 1: Atmosphere and Plant*. Inst. Eng. and Tech., pp. 1–22.
- Sauer J and Muñoz-Esparza D (2020) The FastEddy® resident-GPU accelerated large-eddy simulation framework: Model formulation, dynamical-core validation and performance benchmarks. *Journal of Advances in Modeling Earth Systems* 12(11): e2020MS002100.
- Schalkwijk J, Jonker H, Siebesma PA and Van Meijgaard E (2015) Weather forecasting using GPU-based large-eddy simulations. *Bulletin of the American Meteorological Society* 96(5): 715–723. URL <https://doi.org/10.1175/BAMS-D-14-00114.1>.
- Schumann U (1975a) Subgrid scale model for finite difference simulations of turbulent flows in plane channels and annuli. *Journal of Computational Physics* (18): 376–404.
- Schumann U (1975b) Subgrid scale model for finite difference simulations of turbulent flows in plane channels and annuli. *Journal of Computational Physics* 18(4): 376–404. DOI:[https://doi.org/10.1016/0021-9991\(75\)90093-5](https://doi.org/10.1016/0021-9991(75)90093-5).
- Smagorinsky J (1963) General circulation experiments with the primitive equations. *Monthly Weather Review* 91(3): 99–164. URL [https://doi.org/10.1175/1520-0493\(1963\)091<0099:GCEWTP>2.3.CO;2](https://doi.org/10.1175/1520-0493(1963)091<0099:GCEWTP>2.3.CO;2).
- Sprague M, Ananthan S, Vijayakumar G and Robinson M (2020) ExaWind: A multifidelity modeling and simulation environment for wind energy. *Journal of Physics: Conference Series* 1452. DOI:10.1088/1742-6596/1452/1/012071. 012071, <https://iopscience.iop.org/article/10.1088/1742-6596/1452/1/012071/pdf>.
- Sprague M, Boldyrev S, Fischer P, Grout R, Gustafson Jr W and Moser R (2017) Turbulent flow simulation at the Exascale: Opportunities and challenges workshop. Technical report, U.S. Department of Energy, Office of Science, Advanced Scientific Computing Research. URL <https://www.nrel.gov/docs/fy17osti/67648.pdf>. Published as Tech. Rep. NREL/TP-2C00-67648 by the National Renewable Energy Laboratory.
- Stolz S, Schlatter P and Kleiser L (2005) High-pass filtered eddy-viscosity models for large-eddy simulations of transitional and turbulent flow. *Physics of Fluids* 17(6): 065103. DOI:10.1063/1.1923048. URL <https://doi.org/10.1063/1.1923048>.
- Sullivan P, Edson J, Hristov T and McWilliams J (2008) Large-eddy simulations and observations of atmospheric marine boundary layers above nonequilibrium surface waves. *Journal of the Atmospheric Sciences* 65(4): 1225–1245.
- Sullivan P, McWilliams J and Moeng C (1994) A subgrid-scale model for large-eddy simulation of planetary boundary-layer flows. *Bound.-Layer Meteor.* 71: 247–276.
- Summit (2018) OLCF. <https://www.olcf.ornl.gov/summit/>.
- Świrydowicz K, Chalmers N, Karakus A and Warburton T (2019) Acceleration of tensor-product operations for high-order finite element methods. *Int. J. of High Performance Comput. App.* 33(4): 735–757.
- Van Heerwaarden C, Van Stratum B, Heus T, Gibbs J, Fedorovich E and Mellado J (2017) MicroHH 1.0: A computational fluid dynamics code for direct numerical simulation and large-eddy

simulation of atmospheric boundary layer flows. *Geoscientific Model Development* 10(8): 3145–3165.

Van Leer B (1977) Towards the ultimate conservative difference scheme. iv. a new approach to numerical convection. *Journal of Computational Physics* 23(3): 276–299. DOI:[https://doi.org/10.1016/0021-9991\(77\)90095-X](https://doi.org/10.1016/0021-9991(77)90095-X). URL <https://www.sciencedirect.com/science/article/pii/002199917790095X>.

Zhang W, Almgren A, Beckner V, Bell J, Blaschke J, Chan C, Day M, Friesen B, Gott K, Graves D, Katz M, Myers A, Nguyen T, Nonaka A, Rosso M, Williams S and Zingale M (2019) AMReX: a framework for block-structured adaptive mesh refinement. *Journal of Open Source Software* 4(37): 1370. DOI:[10.21105/joss.01370](https://doi.org/10.21105/joss.01370). URL <https://doi.org/10.21105/joss.01370>.